Three-dimensional multi-relaxation-time lattice Boltzmann front-tracking method for two-phase flow*

Hai-Qiong Xie(谢海琼)[1,2], Zhong Zeng(曾忠)[1,2,3,†], and Liang-Qi Zhang(张良奇)[1,2]

[1] *State Key Laboratory of Coal Mine Disaster Dynamics and Control, Chongqing University, Chongqing* 400044, *China*
[2] *Department of Engineering Mechanics, Chongqing University, Chongqing* 400044, *China*
[3] *Chongqing Key Laboratory of Heterogeneous Material Mechanics, Chongqing University, Chongqing* 400044, *China*

(Received 13 July 2015; revised manuscript received 10 September 2015; published online 30 November 2015)

We developed a three-dimensional multi-relaxation-time lattice Boltzmann method for incompressible and immiscible two-phase flow by coupling with a front-tracking technique. The flow field was simulated by using an Eulerian grid, an adaptive unstructured triangular Lagrangian grid was applied to track explicitly the motion of the two-fluid interface, and an indicator function was introduced to update accurately the fluid properties. The surface tension was computed directly on a triangular Lagrangian grid, and then the surface tension was distributed to the background Eulerian grid. Three benchmarks of two-phase flow, including the Laplace law for a stationary drop, the oscillation of a three-dimensional ellipsoidal drop, and the drop deformation in a shear flow, were simulated to validate the present model.

Keywords: multi-relaxation-time lattice Boltzmann method, front-tracking method, surface tension, two-phase flow

PACS: 47.61.Jd, 05.20.Dd **DOI:** 10.1088/1674-1056/25/1/014702

1. Introduction

The immiscible two-phase flow with an interface appears immensely in both industrial and natural processes, which drives the development in modeling and simulating the two-phase flow. The main difficulty associated with the numerical simulation is modeling the dynamical interface and computing accurately the surface tension. Traditionally, the macroscopic Navier–Stokes (N–S) equations for the two-phase flow are solved together with a proper technique to update the interface location between different phases. There are three commonly used techniques to capture the interface, including the front-tracking method,[1] the volume of fluid (VOF) method,[2] and the level set method.[3] Each method has its own advantages. The front-tracking method represents the interface in a Lagranian fashion and the surface tension is implemented directly at the interface location, thus the front-tracking method captures explicitly the dynamic interface. VOF and level set methods deal naturally the breaking and coalescing interface, and both methods solve an advection equation to capture the interface in an Eulerian grid.

In the above mentioned models for the two-phase flow, the flow field is represented by solving directly the incompressible N–S equations. More recently, the lattice Boltzmann method (LBM) has been developed for computational fluid dynamics (CFD). Different from solving directly the N–S equations (second-order non-linear partial differential equations) in the traditional CFD methods, LBM adopts only a first-order partial differential equation as the evolution equation. In addition, LBM has several advantages over the traditional CFD methods, especially in dealing with complex boundaries, incorporating microscopic interactions, and parallelization of the algorithm.[4] Recently, LBM has been widely adopted to simulate the two-phase fluid–structure interaction[5–7] and thermal fluid flows.[8,9]

In the LBM framework, several hybrid methods, which incorporate LBM with interface tracking techniques, have been developed. Mehravaran and Hannani,[10,11] Thommes *et al.*,[12] and Becker *et al.*[13] incorporated LBM with the level set method to simulate the immiscible two-phase flow. In their hybrid method, the flow fields are simulated by LBM with a BGK operator, and the level set method is applied to capture the evolution of the interface between two fluids. Lallemand *et al.*[14] proposed a hybrid method, in which the two-dimensional flow field is solved by LBM using an Eulerian grid and the interface of two fluids is tracked by using a Lagrangian grid.

Inspired by the hybrid model for the two-phase flow, in this study, we develop a lattice Boltzmann front-tracking method to study the three-dimensional two-phase flow with a sharp dynamical interface based on our previous work for the two-dimensional flow.[15] The LBM model with a multiple-relaxation-time collision process for better stability is applied to simulate the three-dimensional flow field on an Eulerian grid, an additional Lagrangian grid is adopted to track explic-

*Project supported by the National Natural Science Foundation of China (Grant No. 11572062), the Fundamental Research Funds for the Central Universities, China (Grant No. CDJZR13248801), the Program for Changjiang Scholars and Innovative Research Team in University, China (Grant No. IRT13043), and Key Laboratory of Functional Crystals and Laser Technology, TIPC, Chinese Academy of Sciences.

†Corresponding author. E-mail: zzeng@cqu.edu.cn

© 2016 Chinese Physical Society and IOP Publishing Ltd

itly the interface motion, and an indicator function is introduced to update the fluid properties. Three verification cases are conducted for both static and dynamical interfaces.

2. Numerical methods

In this section, three basic parts of our hybrid LBM approach are introduced. The flow field is solved by the multi-relaxation-time LBM, the front-tracking method is adopted to capture the dynamical interface, and the surface tension is implemented directly on the interface.

2.1. LBM model for flow field

The LBM model has three ingredients. The first ingredient is a discrete phase space defined by a regular lattice together with a set of symmetric discrete velocities $\{\boldsymbol{e}_\alpha|\alpha=0,1,\ldots,N\}$ and density distribution functions $\{f_\alpha|\alpha=0,1,\ldots,N\}$. The second ingredient includes a collision matrix $\boldsymbol{S}$ and equilibrium distribution functions $\{f_\alpha^{\rm eq}|\alpha=0,1,\ldots,N\}$. The third ingredient is the evolution equation

$$\boldsymbol{f}(\boldsymbol{x}+\boldsymbol{e}_\alpha\delta_t,t+\delta_t)-\boldsymbol{f}(\boldsymbol{x},t)=-\boldsymbol{S}[\boldsymbol{f}(\boldsymbol{x},t)-\boldsymbol{f}^{\rm eq}(\boldsymbol{x},t)], \quad (1)$$

where $\boldsymbol{S}$ is the collision matrix. In the velocity space, the full matrix $\boldsymbol{S}$ results in the difficulty to implement the collision step. The full collision matrix in the moment space can be transformed into a diagonal matrix, which supports the convenience in performing the collision process.[16–18] Equation (1) is transformed to

$$\begin{aligned}&\boldsymbol{f}(\boldsymbol{x}+\boldsymbol{e}_\alpha\delta_t,t+\delta_t)-\boldsymbol{f}(\boldsymbol{x},t)\\ &=-\boldsymbol{M}^{-1}\widetilde{\boldsymbol{S}}[\boldsymbol{m}(\boldsymbol{x},t)-\boldsymbol{m}^{\rm eq}(\boldsymbol{x},t)],\end{aligned} \quad (2)$$

where $\boldsymbol{m}(\boldsymbol{x},\mathrm{t})$ and $\boldsymbol{m}^{\rm eq}(\boldsymbol{x},\mathrm{t})$ are moments and their corresponding equilibriums, and $\widetilde{\boldsymbol{S}}$ is a diagonal matrix whose components represent the relaxation times of the moments. The transformation between the velocity space and the moment space is achieved by using matrix $\boldsymbol{M}$, which serves as a transformation matrix and maps the distribution functions $\boldsymbol{f}(\boldsymbol{x},t)$ to their moments as

$$\begin{aligned}\boldsymbol{m}&=\boldsymbol{M}\boldsymbol{f},\\ \boldsymbol{f}&=\boldsymbol{M}^{-1}\boldsymbol{m}.\end{aligned} \quad (3)$$

The transformation matrix $\boldsymbol{M}$ is constructed via the Gram–Schmidt orthogonalization procedure from some polynomials of the discrete velocities component.

In this work, the D3Q19 model is adopted as shown in Fig. 1, and the particle velocity directions are

$$\boldsymbol{e}_\alpha=\begin{cases}(0,0,0)\,c, & \alpha=0;\\ (\pm1,0,0)\,c,(0,\pm1,0)\,c,(0,0,\pm1)\,c, & \alpha=1,2,\ldots,6;\\ (\pm1,\pm1,0)\,c,(\pm1,0,\pm1)\,c,(0,\pm1,\pm1)\,c, & \alpha=7,8,\ldots,18;\end{cases} \quad (4)$$

where $c=\delta_x/\delta_t$ is the lattice velocity.

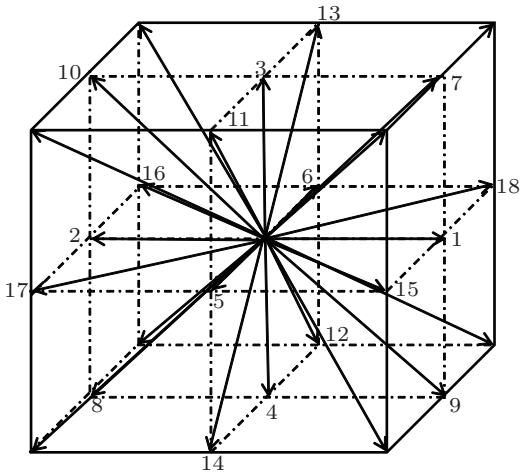


Fig. 1. Illustration of the D3Q19 lattice.

The equilibrium distribution moments $\boldsymbol{m}^{\rm eq}$ are related to the conserved moments as

$$e^{\rm eq}=-11\delta\rho+\frac{19}{\rho_0}\boldsymbol{j}\cdot\boldsymbol{j},\quad \varepsilon^{\rm eq}=3\delta\rho-\frac{11}{2\rho_0}\boldsymbol{j}\cdot\boldsymbol{j},$$

$$\begin{aligned}&q_x^{\rm eq}=-\frac{2}{3}j_x,\quad q_y^{\rm eq}=-\frac{2}{3}j_y,\quad q_z^{\rm eq}=-\frac{2}{3}j_z,\\ &p_{xx}^{\rm eq}=\frac{1}{3\rho_0}\left(2j_x^2-j_y^2-j_z^2\right),\quad p_{ww}^{\rm eq}=\frac{\left(j_y^2-j_z^2\right)}{\rho_0},\\ &p_{xy}^{\rm eq}=\frac{j_yj_z}{\rho_0},\quad p_{yz}^{\rm eq}=\frac{j_yj_z}{\rho_0},\quad p_{xz}^{\rm eq}=\frac{j_xj_z}{\rho_0},\\ &\pi_{xx}^{\rm eq}=-\frac{1}{2}p_{xx}^{\rm eq},\quad \pi_{ww}^{\rm eq}=-\frac{1}{2}p_{ww}^{\rm eq},\\ &m_x^{\rm eq}=m_y^{\rm eq}=m_z^{\rm eq}=0.\end{aligned} \quad (5)$$

The nineteen equilibrium distribution moments of this model are

$$\begin{aligned}\boldsymbol{m}^{\rm eq}=&\left[\delta\rho,\mathrm{e}^{\rm eq},\varepsilon^{\rm eq},j_x,q_x^{\rm eq},j_y,q_y^{\rm eq},j_z,q_z^{\rm eq},3p_{xx}^{\rm eq},\right.\\ &\left.3\pi_{xx}^{\rm eq},p_{ww}^{\rm eq},\pi_{ww}^{\rm eq},p_{xy}^{\rm eq},p_{yz}^{\rm eq},p_{zx}^{\rm eq},m_x^{\rm eq},m_y^{\rm eq},m_z^{\rm eq}\right]^{\rm T},\end{aligned} \quad (6)$$

where $\boldsymbol{j}=(j_x,j_y,j_z)$ is the momentum, $q_{x,y,z}^{\rm eq}$ are the components of the energy flux, $p_{xx}^{\rm eq}$, $\pi_{xx}^{\rm eq}$, $p_{ww}^{\rm eq}$, $\pi_{ww}^{\rm eq}$, $p_{xy}^{\rm eq}$, $p_{yz}^{\rm eq}$, and $p_{zx}^{\rm eq}$ are the components of the symmetric traceless viscous stress tensor, and $m_{x,y,z}^{\rm eq}$ are parts of a third-rank tensor. The collision matrix $\tilde{\boldsymbol{S}}$ in the moment space is

$$\begin{aligned}\tilde{\boldsymbol{S}}=&\,\mathrm{diag}(s_0,s_1,s_2,s_3,s_4,s_5,s_6,s_7,s_8,s_9,s_{10},\\ &s_{11},s_{12},s_{13},s_{14},s_{15},s_{16},s_{17},s_{18}).\end{aligned} \quad (7)$$

The parameters s_0, s_3, s_5, and s_7 are the relaxation times corresponding to the collision invariants. The parameters s_9, s_{11}, s_{13}, and s_{15} are related to the kinematic viscosity ν by $s_9 = s_{11} = s_{13} = s_{15} = 2/\left(1+2\nu/c_s^2\right)$, where $c_s = 1/\sqrt{3}c$.

The fluid macroscopic fluctuation density $\delta\rho$ and velocity $\boldsymbol{u}$ are computed from the moments of the distribution functions as

$$\delta\rho = \sum_{\alpha} f_{\alpha}, \tag{8}$$

$$\boldsymbol{u} = \frac{1}{\rho_0}\sum_{\alpha} \boldsymbol{e}_{\alpha} f_{\alpha}. \tag{9}$$

2.2. Front-tracking method

When the evolution equation (2) is solved numerically on an Eulerian grid, the fluid properties, i.e., density and viscosity, on this grid are required. In terms of the two-phase flow, each phase is assumed as an incompressible flow, and the fluid properties are taken as constant in each phase. Thus the properties of the fluid are physically discontinuous across the interface, and this discontinuity at grid points adjacent to the interface results in many difficulties in simulating numerically the two-phase flow. In order to simulate accurately the interface movement, Tryggvason *et al.*[1] adopted an Eulerian grid as a background grid to solve the governing equations of flow, and applied an additional Lagrangian grid to track explicitly the interface motion. The discontinuities across the interface are distributed from the interface to the background grid, and continuous distributions of the fluid properties can be reconstructed on the Eulerian grid. In this study, the entire flow domain is solved by only one MRT LBM evolution equation (2) and the different fluids are treated as one fluid with varying properties across the interface. The mixed Eulerian and Lagrangian grids are exhibited in Fig. 2.

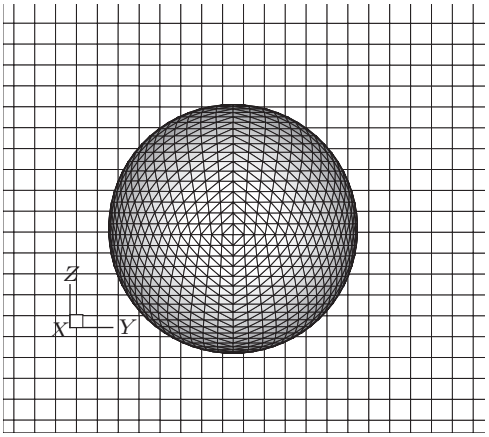


Fig. 2. The Eulerian grid for flow field and Lagrangian grid for interface.

The reconstruction of the fluid properties $b(\boldsymbol{x},t)$ at time t in the whole background grid is achieved through constructing an indicator function $I(\boldsymbol{x},t)$. Let this indicator function be zero in one phase and one in another phase, then we can define

$$b(\boldsymbol{x},t) = b_1 + (b_0 - b_1) I(\boldsymbol{x},t), \tag{10}$$

where $b(\boldsymbol{x},t)$ is either fluid density or viscosity, and the subscripts 0 and 1 refer to fluid 1 and fluid 2, respectively. According to the interface location, the indicator function $I(\boldsymbol{x},t)$ is obtained by solving the following Poisson equation:

$$\nabla^2 I(\boldsymbol{x},t) = \nabla\cdot\boldsymbol{G}(\boldsymbol{x},t). \tag{11}$$

The Poisson equation is solved by a standard second-order centered difference method, and the linear equation is solved with a traditional successive-over-relaxation method. Here $\boldsymbol{G}(\boldsymbol{x},t)$ is related to the interface location and normal

$$\boldsymbol{G}(\boldsymbol{x},t) = \int_{\Gamma} \boldsymbol{n}_{\mathrm{f}} D(\boldsymbol{x}-\boldsymbol{x}_{\mathrm{f}})\,\mathrm{d}s, \tag{12}$$

where $\boldsymbol{n}_{\mathrm{f}}$ is the unit normal vector of the interface, Γ represents the interface between the two phases, $\boldsymbol{x}_{\mathrm{f}}$ is the coordinates of the interface points, and $D(\boldsymbol{x}-\boldsymbol{x}_{\mathrm{f}})$ is a distribution function for the interface. In this study, we adopt the traditional Peskin distribution function to approximate the $D(\boldsymbol{x}-\boldsymbol{x}_{\mathrm{f}})$ function

$$D(\boldsymbol{x}-\boldsymbol{x}_{\mathrm{f}}) = \begin{cases} d_1(\boldsymbol{x}-\boldsymbol{x}_{\mathrm{f}}), & \text{if } |\boldsymbol{x}-\boldsymbol{x}_{\mathrm{f}}| \le 1; \\ 1/2 - d_1(2-|\boldsymbol{x}-\boldsymbol{x}_{\mathrm{f}}|), & \text{if } 1 < |\boldsymbol{x}-\boldsymbol{x}_{\mathrm{f}}| < 2; \\ 0, & \text{if } |\boldsymbol{x}-\boldsymbol{x}_{\mathrm{f}}| \ge 2; \end{cases} \tag{13}$$

$$d_1(\boldsymbol{r}) = \frac{3-2|r|+\sqrt{1+4|r|-4r^2}}{8}. \tag{14}$$

The partial derivatives in Eq. (11) are computed as

$$\frac{\partial \boldsymbol{G}}{\partial \boldsymbol{x}} = \frac{1}{2c_s^2\delta t}\sum_{\alpha\neq 0} w_{\alpha}\boldsymbol{e}_{\alpha}\left[G(\boldsymbol{x}+\boldsymbol{e}_{\alpha}\delta t) - G(\boldsymbol{x}-\boldsymbol{e}_{\alpha}\delta t)\right], \tag{15}$$

where w_{α} is the weight coefficient

$$w_{\alpha} = \begin{cases} 1/3, & \alpha = 0; \\ 1/18, & \alpha = 1,2,\ldots,6; \\ 1/36, & \alpha = 7,8,\ldots,18. \end{cases} \tag{16}$$

This discretization is based on the lattice-based stencil, instead of the standard stencil based on the coordinate directions. A smooth indicator function can be constructed by solving the Poisson equation (11). This indicator function is zero in one phase, varies continuously from zero to one in a certain thickness region, and one in another phase.

The governing equation (2) is solved on the stationary background grid. And then the velocity of the interface makers is interpolated from the flow field on the background grid. Subsequently, the interface makers move in a Lagrangian manner from a position $\boldsymbol{x}_{\mathrm{f}}^{n}$ at the n time step to a position $\boldsymbol{x}_{\mathrm{f}}^{n+1}$ at the $n+1$ time step

$$\boldsymbol{u}_{\mathrm{f}}(\boldsymbol{x}_{\mathrm{f}},t) = \sum_{x} \boldsymbol{u}(\boldsymbol{x},t) D(\boldsymbol{x}-x_{\mathrm{f}}), \tag{17}$$

$$\boldsymbol{x}_{\mathrm{f}}^{n+1} = \boldsymbol{x}_{\mathrm{f}}^{n} + \boldsymbol{u}_{\mathrm{f}}^{n}\delta_t, \tag{18}$$

where the velocity interpolation is carried out using the same distribution function as Eq. (13).

As the interface makers move, the interface grid resolution may change, which has a strong effect on the information exchange between Lagrangian grid and Eulerian grid. Therefore, an adaptive Lagrangian grid is adopted to maintain the resolution during the simulation. In this study, restructuring the Lagrangian grid for the interface consists of two operations, edge split and edge deletion. For a short edge, the edge is removed, and for a long edge, an additional maker is placed in the middle of the edge. Generally, we take the maximum edge length as the Eulerian grid size, and the minimum edge length as 0.3 times the Eulerian grid size.

2.3. Surface tension

Calculating accurately the surface tension is a great challenge in simulating the two-phase flow. In this study, the surface tension is computed from the tensile forces on the three edges of all interface elements m (see Fig. 3)

$$\boldsymbol{F}_m = \sum_k \sigma(\boldsymbol{t}_k \times \boldsymbol{n}_k), \quad k = 1,2,3, \tag{19}$$

where $\boldsymbol{t}_k$ is the tangent vector of the edge shared by element m and neighboring element k, and $\boldsymbol{n}_k$ is its unit normal vector. The summation in Eq. (19) is carried out over all three edges of the element m. The three tangent vectors $\boldsymbol{t}_k$ of the element m can be computed directly from the known positions of the three corner points of the element. Once the tangent vectors are obtained, the unit normal vectors can be found from the cross-product of two different tangent vectors.

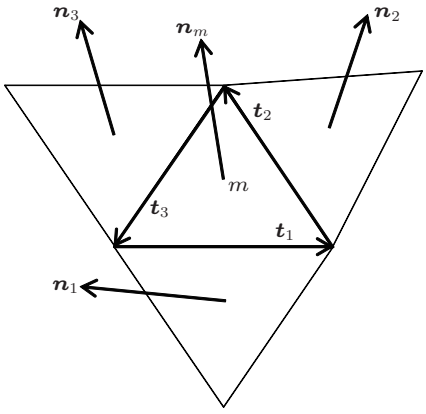


Fig. 3. The surface tension on element m with three neighboring surface elements.

3. Simulation and results

In this section, the three-dimensional MRT LBM model incorporating front-tracking technique is validated by three benchmark cases, including the Laplace law for a stationary drop, the oscillation of a three-dimensional ellipsoidal drop, and the drop deformation in a shear flow. Unless otherwise specified, we express the results in lattice units.

3.1. Laplace law of a stationary drop

Initially, a three-dimensional spherical drop locates at the center of the domain, and a homogenous pressure is set initially. The periodic boundary conditions are imposed at all boundaries. According to the Laplace law, the pressure difference across the drop interface at equilibrium is related to the surface tension

$$\Delta p = p_{\mathrm{in}} - p_{\mathrm{out}} = \frac{2\sigma}{R}, \tag{20}$$

where R is the drop radius, and p_{in} and p_{out} are the pressures inside and outside of the drop, respectively. The pressure inside the drop is measured by averaging the pressures at all lattice points inside the spherical drop at $0.7R$, and the outside pressure is measured by averaging the pressures at all lattice points at $1.3R$ away from the drop center.

In this numerical computation, we consider four different radii 10, 12, 14, and 16. The corresponding three-dimensional domain is discretized by $6R \times 6R \times 6R$ lattice units. In all the cases, the surface tension σ is set to be 0.01, the kinematic viscosity ν is equal to 0.1, and two different density ratios are adopted. Table 1 demonstrates the comparison between the simulating pressure difference $\Delta p_{\mathrm{simulation}}$ across the drop interface and the theoretical pressure difference $\Delta p_{\mathrm{theory}}$ computing from Eq. (20). The error ($E = \frac{|\Delta p_{\mathrm{theory}} - \Delta p_{\mathrm{simulation}}|}{\Delta p_{\mathrm{theory}}} \times 100\%$) for the pressure difference across the interface is within 3.5%. In addition, we take the two-dimensional diffusive model[19] as the reference. The maximum error compared to the theoretical solution is 12% for $R = 40$ lattice units in Ref. [19], and the maximum error compared to the theoretical solution is less than 4% in the present model. In fact, with increasing drop radius, the error compared to the theoretical value decreases apparently. Therefore, a relatively large drop is required to achieve a reasonable precision in the diffusive model,[19] because the interface transition zone in the diffusive model is thicker than that in the present interface tracking method. Finally, the variations of the drop volume are also investigated, the results indicate that the decrement of drop volume in the equilibrium is less than 0.5% compared to the initial volume.

Table 1. Pressure differences across the interface for different drop radii from LBM simulations and the theoretical solution based on the Laplace law.

		$\gamma = 5$		$\gamma = 10$	
R	$\Delta p_{\mathrm{theory}}$	$\Delta p_{\mathrm{Laplace}}$	E/%	$\Delta p_{\mathrm{Laplace}}$	E/%
12	1.667×10^{-3}	1.608×10^{-3}	3.53	1.597×10^{-3}	4.19
14	1.429×10^{-3}	1.387×10^{-3}	2.94	1.375×10^{-3}	3.78
16	1.250×10^{-3}	1.222×10^{-3}	2.24	1.215×10^{-2}	2.80
18	1.111×10^{-3}	1.095×10^{-3}	1.60	1.089×10^{-2}	1.98

3.2. Oscillation of a three-dimensional ellipsoidal drop

The oscillation of a three-dimensional ellipsoidal drop, which immerses in another fluid, is considered. The frequency of the oscillatory drop is given in Ref. [20]

$$\omega_n = \omega_n^* - \frac{1}{2}\chi\omega_n^{*1/2} + \frac{1}{4}\chi^2, \tag{21}$$

where ω_n is the angular frequency, and ω_n^* is Lamb's natural frequency expressed as

$$\omega_n^* = \left(\frac{n(n+1)(n-1)(n+2)}{R_E^3(n\rho_o + (n+1)\rho_i)}\sigma\right)^{1/2}, \tag{22}$$

with R_E being the equilibrium radius of the drop. The parameter χ is given by

$$\chi = \frac{(2n+1)^2(\mu_o\mu_i\rho_o\rho_i)^{1/2}}{\sqrt{2}R_E[n\rho_o + (n+1)\rho_i]\left[(\rho_i\mu_i)^{1/2} + (\rho_o\mu_o)^{1/2}\right]}, \tag{23}$$

where μ_o and μ_i are the dynamic viscosities of the two fluids, respectively. The theoretic expression for the period T_{theory} is obtained from Eq. (21) through $T_{\text{theory}} = 2\pi/\omega_2$ with $n = 2$.

Table 2. Comparison of the oscillation periods between the analytical solutions and the LBM results for different viscosities.

	$\sigma = 0.01$			$\sigma = 0.005$		
ν	T_{anal}	T_{LBM}	E/%	T_{anal}	T_{LBM}	E/%
0.005	1418	1400	1.26	2022	2040	0.89
0.01	1443	1430	0.90	2064	2105	1.99
0.02	1478	1492	0.95	2122	2180	2.73

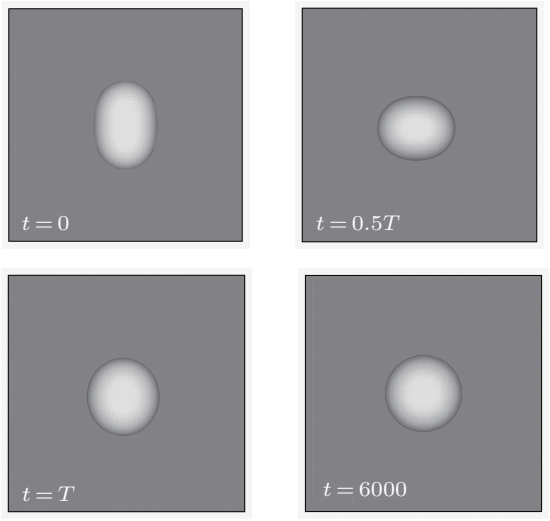


Fig. 4. Configurations of an oscillating drop at different time.

Initially, the minimum and the maximum radii of the ellipsoidal drop are 11 and 13, respectively. The ellipsoidal drop is placed in the domain center, and the domain is $72 \times 72 \times 72$ lattice units. Table 2 indicates that the simulated periods coincide well with the theoretic periods T_{theory} for different viscosities and different surface tensions. The maximum relative error for $\sigma = 0.01$ is 1.26% and the maximum relative error for $\sigma = 0.005$ is 2.73%. Figure 5 exhibits the interface locations of the oscillating drop as a function of time for three different viscosities. Due to the surface tension and the viscous force, the ellipsoidal drop will reach the equilibrium state with a spherical shape, the spherical radius at equilibrium is $R = 11.88$. In addition, it takes more time to reach the equilibrium state with a smaller viscosity.

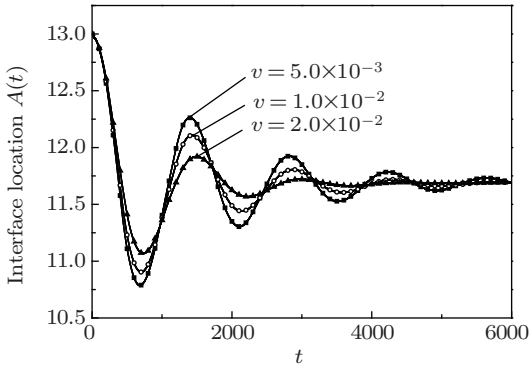


Fig. 5. Interface location of an oscillating drop as a function of time for different kinematic viscosities.

3.3. Drop deformation in a shear flow

In this section, a three-dimensional numerical simulation is performed on the classical Taylor experiment, the drop deformation within a shear flow as illustrated in Fig. 6. The drop deformation depends on two dimensionless parameters, the Reynolds and the capillary numbers, which are defined as

$$Re = \frac{\gamma R^2}{\nu}, \tag{24}$$

$$Ca = \frac{\gamma R\nu}{\sigma}, \tag{25}$$

where $\gamma = U_0/H$ is the shear rate and H is the half height of the parallel plates. For small Re and Ca, the drop eventually tends to be in a steady state, and a parameter D_f is adopted to characterize the drop deformation

$$D_f = \frac{L-B}{L+B}, \tag{26}$$

where L and B are the largest and the smallest distances from the drop surface to its center (major and minor axes). Taylor[21] presented the theoretic result for small D_f

$$D_f = \frac{35}{32}Ca. \tag{27}$$

The parameters are adopted as $\rho_i = \rho_o = 1$, $\sigma = 0.01$, $Re = 0.1$, and the viscosity of the drop is equal to the surrounding fluid. The capillary number varies from 0.05 to 0.30. The computational domain is $12R \times 6R \times 6R$ lattice units. Figure 7 indicates that the deformation parameters D_f in this simulation are in good agreement with the theoretic Taylor relation at small capillary numbers. Figure 8 shows that the deformation of the drop is more obvious with a larger capillary

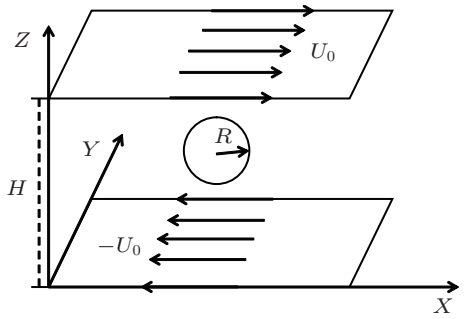


Fig. 6. Drop deformation within a shear flow.

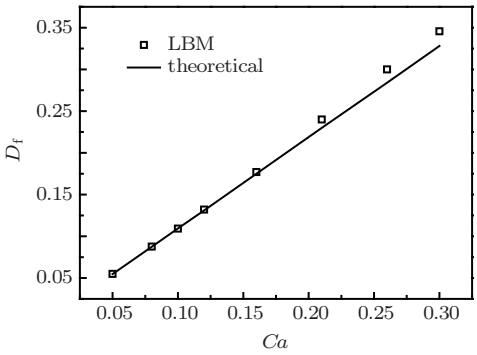


Fig. 7. Taylor deformation parameter D_f as a function of the capillary number at $Re = 0.1$.

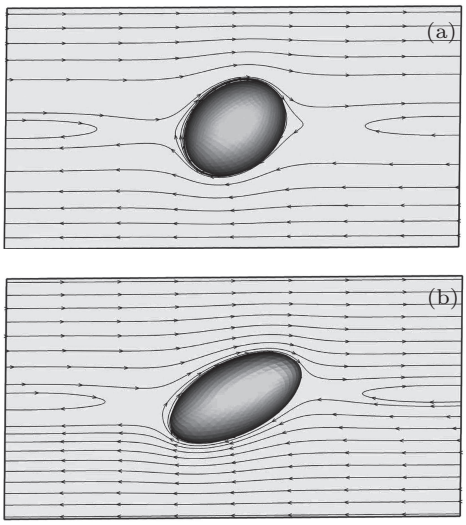


Fig. 8. Velocity field in the x–z plane and the deformed droplet: (a) $Ca = 0.1$, (b) $Ca = 0.26$.

number. For $Ca = 0.1$, the deformation parameter obtained from the simulation is $D_f = 0.109$, and for $Ca = 0.26$, the deformation parameter is $D_f = 0.309$.

4. Conclusion

We have developed an MRT lattice Boltzmann model incorporating the front-tracking technique to simulate the two-phase flow with a dynamical interface. The flow field was simulated by LBM method on an Eulerian grid, and an adaptive unstructured triangular Lagrangian grid was applied to track explicitly the interface motion. Three benchmark cases were simulated to validate this model. In the benchmark of a three-dimensional spherical drop, the Laplace law is well satisfied with the simulated pressure difference across the interface. In the benchmark of an oscillating ellipsoidal drop, the simulated oscillatory period is consistent with the theoretical solution. In the benchmark of the drop deformation in a shear flow, the simulated drop deformation coincides well with the theoretical solution for small capillary number.

References

[1] Unverdi S O and Tryggvason G 1992 *J. Comput. Phys.* **100** 25
[2] Hirt C W and Nichols B D 1981 *J. Comput. Phys.* **39** 201
[3] Sussman M, Smereka P and Osher S J 1994 *J. Comput. Phys.* **114**
[4] Chen S and Doolen G D 1998 *Annu. Rev. Fluid Mech.* **30** 329
[5] Yi H H, Yang X F, Wang C F and Li H B 2009 *Chin. Phys. B* **18** 2878
[6] Yi H H, Fan L J, Yang X F and Li H B 2009 *Chin. Phys. Lett.* **26**
[7] Cai J and Huai X L 2009 *Chin. Phys. Lett.* **26**
[8] Zhong C W, Xie J F, Zhou C S, Xiong S W and Yin D C 2009 *Chin. Phys. B* **18** 4083
[9] Ran Z 2009 *Chin. Phys. B* **18** 2159
[10] Mehravaran M and Hannani S K 2011 *Scientia Iranica B* **18** 231
[11] Mehravaran M and Hannani S K 2008 *Comput. Methods Appl. Mech. Engrg.* **198** 223
[12] Thommes G, Becker J, Junk M, Vaikuntam AK, Kehrwald D, Klar A, Steiner K and Wiegmann A 2009 *J. Comput. Phys.* **228** 1139
[13] Becker J, Junk M, Kehrwald D, Thömmes G and Yang Z X 2009 *Comput. Math. Appl.* **58** 950
[14] Lallemand P, Luo LS and Peng Y 2007 *J. Comput. Phys.* **226** 1367
[15] Xie H Q, Zeng Z and Zhang L Q 2012 *Chin. Phys. B* **21** 124703
[16] D'Humieres D 1992 *Prog. Astronaut. Aeronaut.* **159** 450
[17] Lallemand P and Luo L S 2003 *Phys.Rev. E* **68** 036706
[18] Lallemand P and Luo L S 2000 *Phys. Rev. E* **61** 6546
[19] Kannan N, Premnath and John A 2007 *J. Comput. Phys.* **224** 539
[20] McCracken M E and Abraham J 2005 *Phys. Rev. E* **71** 036701
[21] Taylor G I 1932 *Proc. R. Soc. Ser. A* **138** 41